Measurement and Classification of Low-Grazing-Angle Radar Sea Spikes

Yong Liu, *Member, IEEE*, Stephen J. Frasier, *Member, IEEE*, and Robert E. McIntosh, *Fellow, IEEE*

Abstract—High-resolution dual-polarization X-band images of the ocean surface were obtained at a grazing angle of about 3°. Area extensive imaging allowed us to study backscatter properties of sea spikes and to compare radar measurements with visual surface features evident from video recordings. The vertically polarized radar images consist of distributed scatter whose amplitude and Doppler velocity are modulated by larger scale gravity waves consistent with Bragg scattering and composite surface theory (CST). The horizontally polarized radar images are dominated by spatially discrete scattering centers (or sea spikes) moving at velocities comparable to the phase velocities of gravity waves beyond the spectral peak. These sea spikes also exist in the corresponding V-pol radar images, but are less prominent due to the dominant Bragg backscatter. Sea spikes are characterized by polarization ratios H/V that often exceed unity, typically by about 5 dB. Comparison of the larger spikes with simultaneous co-registered video recording of the surface indicates that approximately 30% of observed sea spikes are associated with actively breaking waves (whitecaps) while the remainder are identified with "steep" wave features. By classifying the larger sea spikes according to their corresponding surface features, we find Doppler velocities for sea spikes due to whitecaps noticeably faster (about 50%) than other sea spikes, though the distributions for both overlap significantly. We also find little measurable difference in the polarization ratios of the two classes of sea spikes as observed on the open ocean.

Index Terms—Sea surface electromagnetic scattering.

I. INTRODUCTION

UNDERSTANDING the physics of microwave backscatter from the ocean surface in the low-grazing-angle (LGA) regime is important in two aspects. First, for surveillance radar, optimal target detection requires knowledge of the statistics of the background clutter. Second, the use of radar as a tool to study the ocean surface requires understanding of the scattering mechanisms to interpret radar data and to relate it to oceanic parameters. For over three decades scientists have attempted to explain LGA radar backscatter. Characteristics of LGA backscatter that present particular problems to modelers are the marked differences in horizontally polarized (H) and vertically polarized (V) Doppler properties, and the intermittent and impulsive nature of H-polarized backscatter

with intensities often exceeding those of the corresponding V-polarized signal.

At moderate incidence angles, microwave backscatter is reasonably well described by composite surface theory (CST) [1], [2] where Bragg-resonant capillary-gravity waves ride atop gently undulating long waves. The small scale waves provide the mechanism for the microwave echo, while the larger scale waves are resolved through their modulation of the backscatter. As the incidence angle approaches grazing, however, many have reported that the normalized radar cross section (RCS) for H polarization is much higher than that predicted by CST and the frequency of the Doppler spectrum peak for H polarization is also higher than that for V [3]–[7]. "Sea spikes," a colloquial term to describe strong backscatter events frequently appearing in H polarized high-resolution radar data, have been studied both in the field [8], [9], [27] and the laboratory [10]–[12]. They have been shown to cause broadening of the Doppler spectra, increased frequency of the Doppler spectrum peak, and polarization ratio often exceeding unity. Theoretical models such as wedge diffraction [13], accelerating plumes [14], bound capillary waves [15], and specular reflection have been proposed to explain the observations. Recent experimental evidence indicates that multipath scattering from objects near the surface leads to polarization characteristics similar to those of sea spikes [16].

In this paper, we present a study comparing dual-polarized LGA radar backscatter measurements with simultaneous co-registered video recordings of the surface. The radar data was obtained using the focused phased-array imaging radar (FOPAIR), a high-resolution X-band (10 GHz) phased-array imaging radar described in [17] with modifications for dual-polarization operation. With an image spatial resolution of approximately 2 m, updated at 48–64 frames per second, the radar is able to identify and track scattering features in both space and time. Because the radar is also able to estimate mean Doppler shift at each pixel, it is possible to relate radar imagery to the more traditional Doppler spectrum observations of nonimaging scatterometers. By comparing V- and H-polarized radar images with video recordings of the ocean surface, we infer Doppler and polarization properties of the observed sea-spike events that can be associated with visual surface features. Previous radar-video studies usually involved comparisons of video recordings with time-series of radar backscatter from a small spot on the surface. The area extensive high-resolution radar data presented here permits comparison of both radar and video image features.

Fig. 1.   FOPAIR configuration on the R/P FLIP during the marine boundary layer experiment.

In the following section, the radar system, experimental setup, and data processing procedures are described. Environmental conditions and corresponding radar imagery and Doppler properties are presented in Section III. In Sections IV and V, we compare the radar and video imagery and interpret the results of the classification of observed sea spikes.

II. RADAR SYSTEM AND EXPERIMENTAL SETUP

The radar system consists of two sequentially sampled 64-element receiving antenna arrays, one vertically polarized and one horizontally polarized. Each array employs a co-polarized pyramidal horn transmitter to illuminate the ocean surface. Range resolution is 1.5 m and azimuthal resolution is $0.5°$ within the arrays' $24°$ field of view. This translates to an azimuthal pixel dimension of 1.75 m at 200-m range (the mean range of the data presented in this paper). Peak transmitted power is 200 W, boosted to an effective peak power of 40 kW through pulse compression.

From April 18 to May 8, 1995, the radar was deployed on the R/P FLIP during Phase-II of the marine boundary layer experiment (MBLEX). FLIP was moored at $36.6°$ N, $122.5°$ W, approximately 50-km west of Monterey, CA. The FOPAIR antenna was attached to a boom on the starboard side of FLIP approximately 12 m above the mean water level and was aimed in the direction of the keel of FLIP, nominally North (see Fig. 1). The area of ocean surface imaged by FOPAIR was, therefore, a $24°$ wedge lying between 150 and 246 m, corresponding to grazing angles between 4.2 and $2.8°$, respectively.

Throughout the experiment, the radar was configured to acquire images in pairs with an interimage delay of 2.5 ms. Acquisition time for each image is 0.64 ms during which it is assumed that the motion of the ocean surface is effectively frozen while the short delay between images provides a means for estimating Doppler velocity at each pixel location. The 2.5-ms delay translates to a Doppler velocity Nyquist interval of ± 3.0 ms^{-1}. During this experiment, image pairs were acquired at rates between 48 and 64 Hz in a polarization interleaved format: vertical-vertical (VV), horizontal-horizontal (HH), $\cdots$,

yielding an image-pair (or "frame") rate of 24–32 Hz per polarization.

Radar echoes acquired by the array are stored directly to high-speed disk in an unfocused format. Focused radar images are then generated through postprocessing on a computer work station following the experiment. Once complex radar images are formed, three image products are accumulated: backscattered power, Doppler velocity, and the coherence of the complex backscatter. Letting $V(t)$ and $V(t+\tau)$ represent corresponding pixel values in the complex images of a given pair, the image products are

$$P = \frac{\langle |V(t)|^2 \rangle + \langle |V(t+\tau)|^2 \rangle}{2} \tag{1}$$

$$v = \frac{\lambda}{2} \frac{\arg \langle V(t)V^*(t+\tau) \rangle}{2\pi\tau} \tag{2}$$

$$\rho = \frac{|\langle V(t)V^*(t+\tau) \rangle|}{\sqrt{\langle |V(t)|^2 \rangle \langle |V(t+\tau)|^2 \rangle}} \tag{3}$$

where P, v, and ρ are backscattered power, Doppler velocity, and coherence, respectively, and $\langle \rangle$ denotes averaging over a short time interval. In (2), λ is the radio wavelength and τ is the inter-image delay. For ocean measurements, Doppler velocity is often converted to a horizontal component of Doppler velocity by dividing by the sine of the incidence angle. Near grazing, however, this correction is negligible. The coherence ρ is an indicator of the uncertainty of the Doppler velocity estimate. Measurement of ρ combined with an assumed form for the autocorrelation function of $V(t)$ can be used to estimate Doppler bandwidth of the scattering within the image pixel [18]. Such an approach is commonly used in weather radar applications [19], however, as relatively few samples are averaged in our short time estimates, we use ρ as a qualitative figure-of-merit only. When ρ approaches unity, uncertainty is small implying a narrowband-type scattering during the time interval. When it is low, uncertainty is large implying either a broad instantaneous Doppler bandwidth within the pixel or inadequate signal-to-noise ratio (SNR) when backscattered power levels are low.

With this procedure, backscattered power, Doppler, and coherence were calculated for both polarizations and averaged over 0.25 s (six–eight image pairs, depending upon the frame rate used) yielding simultaneous image sequences of vertically and horizontally polarized backscatter at a 4-Hz update rate. Power images are corrected for the radar's azimuthal antenna pattern and for an inverse cubic range dependence appropriate for pulse-limited operation when viewing a distributed target. Resulting power units are proportional to normalized RCS, $\sigma°$. The two polarizations are co-registered with each other using results from a post-experiment deployment in which the arrays both view a trihedral corner reflector. Power images are not absolutely calibrated, although comparisons between polarizations are permitted through the polarization ratio, H/V.

III. OBSERVATIONS

Meteorological parameters were measured continuously during the experiment. Five-minute averaged winds measured
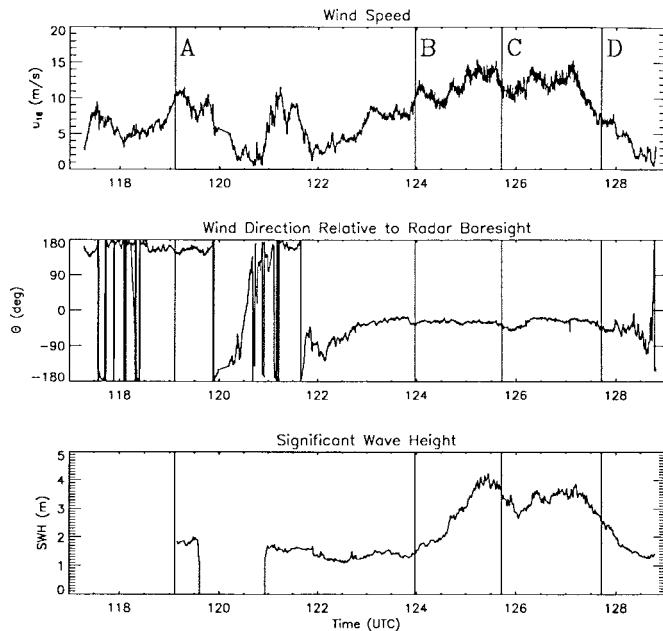
Fig. 2. Wind and wave conditions during MBL experiment. A, B, C and D mark the four cases that are examined in this paper. Wind directions are relative to the radar boresight ($0°$ = upwind).

TABLE I
SUMMARY OF ENVIRONMENTAL PARAMETERS

Case	SWH (m)	F_{pk} (Hz)	Λ_{pk} (m)	C_p (ms^{-1})	$U_{16.5}$ (ms^{-1})
A	1.7	0.26	23	6.0	10.1
B	1.5	0.23	30	6.8	10.6
C	3.6	0.13	92	12.0	12.4
D	2.5	0.13	92	12.0	5.8

at 16.5-m height are shown in Fig. 2 as is significant wave height [(SWH), defined here as four times the rms surface displacement] as measured by a wave wire. From April 27 to 30, winds were predominantly from the south and southeast, with speeds varying from under 5 ms^{-1} to approximately 10 ms^{-1}. Winds shifted on May 2 remaining consistent from the north/northwest developing from under 5 ms^{-1} to over 14 ms^{-1} on May 4 and 6. Winds diminished on May 7 with a subsequent reduction in wave height. In this section, we present representative data from four situations marked in Fig. 2 as A, B, C, and D. These correspond to one downwind–downwave observation [A, April 28] and three upwind–upwave observations: a young sea [B, May 3], a developed sea [C, May 5], and a decaying sea [D, May 7]. Wind and wave parameters for these four cases are given in Table I showing measured wind, wave height, and dominant wave frequency. Dominant wavelengths and phase velocities are calculated using linear theory. We begin with the upwind cases.

A. Radar and Video Imagery

The upper panel of Fig. 3 shows V-polarized radar images for a young sea obtained on May 3. Though the wind has been blowing for over 20 h from northwest (the upper-left corner in the radar images), little development of seas occurred, possibly due to an opposing swell. The wind speed at the time of the radar images was 10 ms^{-1}, just at the onset of significant sea development with frequent whitecapping. The left image is the backscattered power, the middle image is Doppler velocity, and the right image is coherence. The V-polarized imagery shows distributed scattering in which both power and Doppler velocity images show modulations due primarily to the longer waves. Comparisons of power and Doppler time-series indicate that the strongest return is generally associated with the forward faces of the advancing waves. Some shadowing effects appear evident in the areas characterized by low powers, noisy (speckled) velocities, and low coherence values as these areas are generally located behind advancing wave crests. The observed distributed scattering is qualitatively consistent with the CST. Note, however, that local power maxima are usually accompanied by correspondingly high Doppler velocities and, occasionally, by low coherence values implying broad instantaneous Doppler bandwidths. Such a signature is consistent with the "sea spikes" observed in V-polarized backscatter at moderate incidence angles [9].

The lower panel of Fig. 3 shows the corresponding H-polarized images where very little distributed backscatter is evident. Since the predicted Bragg backscatter for H is approximately 30 dB weaker than V at this grazing angle [2], only very localized non-Bragg scatterers contribute to the echo. These are qualitatively consistent with observations of sea spikes. The background in the HH power image represents the noise floor of the radar. The velocity image shows random velocities in areas of little or no scattering consistent with a randomly distributed phase for noise. The coherence image also shows low values virtually everywhere except where scattering is significant.

Features in the radar imagery can be roughly reconciled with features in the corresponding video image shown in Fig. 4. The rectangle in the video frame in Fig. 4(a) marks the approximate location of the radar footprint given the viewing geometry and assuming a flat sea. Some misregistration between radar image features and their apparent sources as discerned from video is inevitable as the sea is never truly flat. This is particularly an issue in higher sea states. Panels (b) and (c) in Fig. 4 show a stretched version of the boxed area and a color composite of the radar power images transformed into the video's coordinate system. V scattering is represented by green intensity and H by red. Where they are of comparable magnitude, the colors combine yielding yellow. Here it is possible to see evidence of non-Bragg scattering events one can associate with visual surface features such as whitecaps or steep wave features.

Figs. 5 and 6 show radar and video images for more developed seas (May 5) and for decaying seas (May 7). First-order image characteristics for these are similar to those for the young sea except for the obvious differences in dominant wavelength and the more pronounced effects of shadowing. Fig. 7 shows radar images for the downwind look. The vertically polarized return is again dominated by distributed scatterer, while the horizontally polarized return consists of sea spikes only. Compared with the upwind cases, sea spikes are less frequent and their backscatter is noticeably weaker.
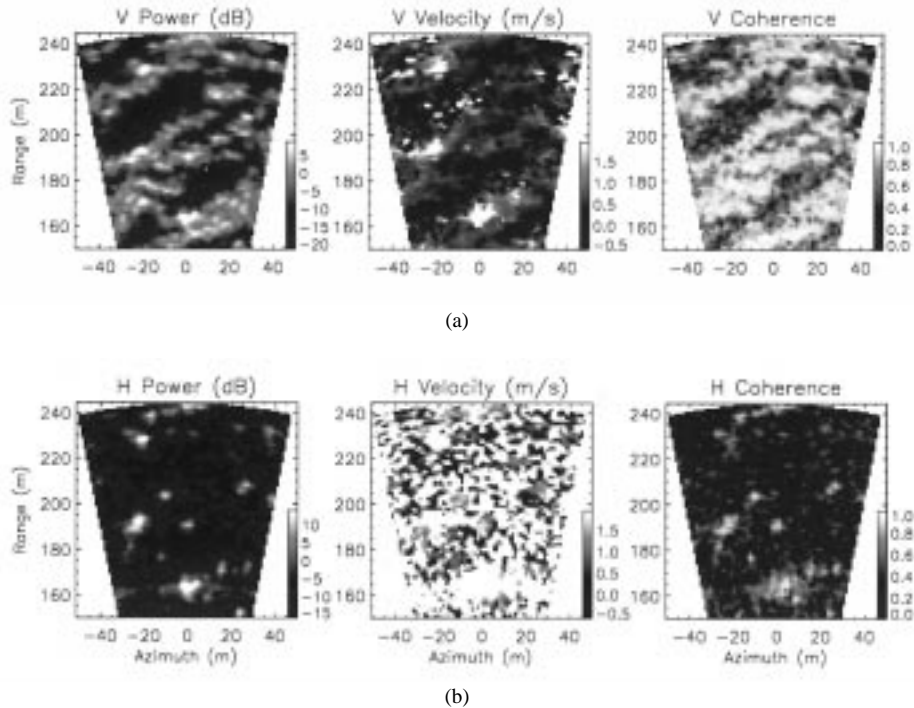
(a)

(b)

Fig. 3.   Radar images for an upwind young sea (Case B). (a) Vertically polarized radar images. (b) Horizontally polarized radar images.

B. Doppler Properties

To compare this imagery with results of other investigators, it is useful to examine the Doppler properties of the backscatter. Doppler spectra are the typical output format of coherent scatterometers used in many ocean scattering studies. Because of the large data bandwidth associated with the imaging radar, it is not feasible to obtain a resolved Doppler spectrum at each pixel location; only a mean Doppler velocity is estimated. However, because there exists both a (short-time) power and a Doppler velocity estimate at each pixel, one can construct a power-weighted Doppler velocity histogram by binning powers by their corresponding Doppler velocities. The resulting distribution of power with Doppler velocity is analogous to a mean Doppler spectrum, though not strictly equivalent. In particular, it does not capture temporal characteristics such as the effects of finite scatterer lifetimes that a Doppler spectrum obtained via Fourier transformation contains. It is worth noting that it can be considered equivalent for the particular case of a slowly frequency modulated waveform with a large modulation index [22], a reasonable signal model for composite-surface scattering in which a narrowband (Bragg) echo from a small spot is amplitude and frequency modulated by the slowly varying long waves. However, since only a portion of the scattering we observe is described by this model, we refer to our "spectra" simply as weighted Doppler distributions.

Fig. 8 shows Doppler distributions calculated for the cases shown in Figs. 3–7. Each distribution is an accumulation over all pixels in an 8-min data record where a frequency independent noise floor has been subtracted from each curve. Solid and dashed curves show the respective Doppler distributions for vertical and horizontal polarizations. In each case, an asymmetric V distribution is accompanied by a
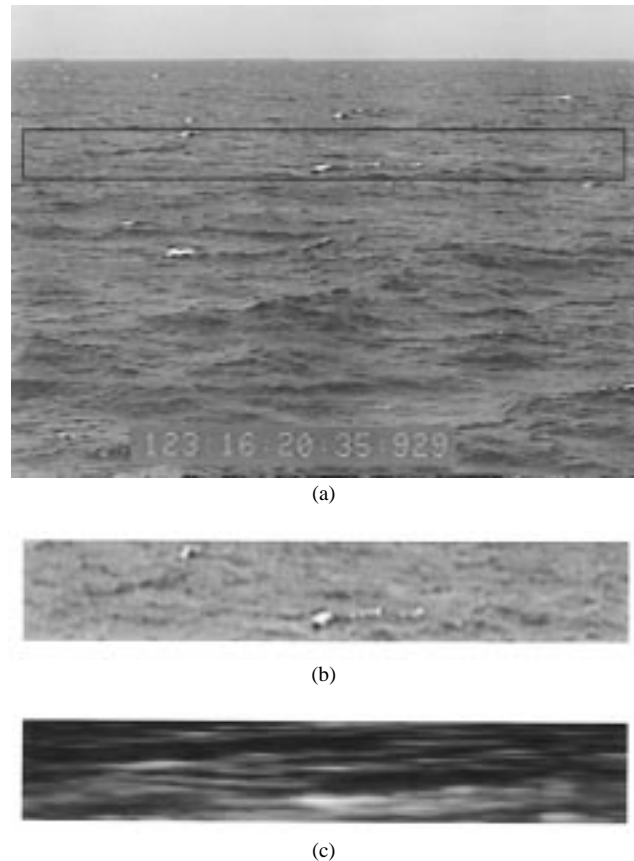

(a)

(b)

(c)

Fig. 4.   Video image corresponding to the radar images in Fig. 3. (a) The overall view where the boxed area indicates the radar footprint. (b) A stretched version of the boxed area. (c) A color-composite of the radar images transformed into video coordinates where H backscatter is coded in red and V backscatter is coded in green. Yellow areas signify both strong H and V backscatter.
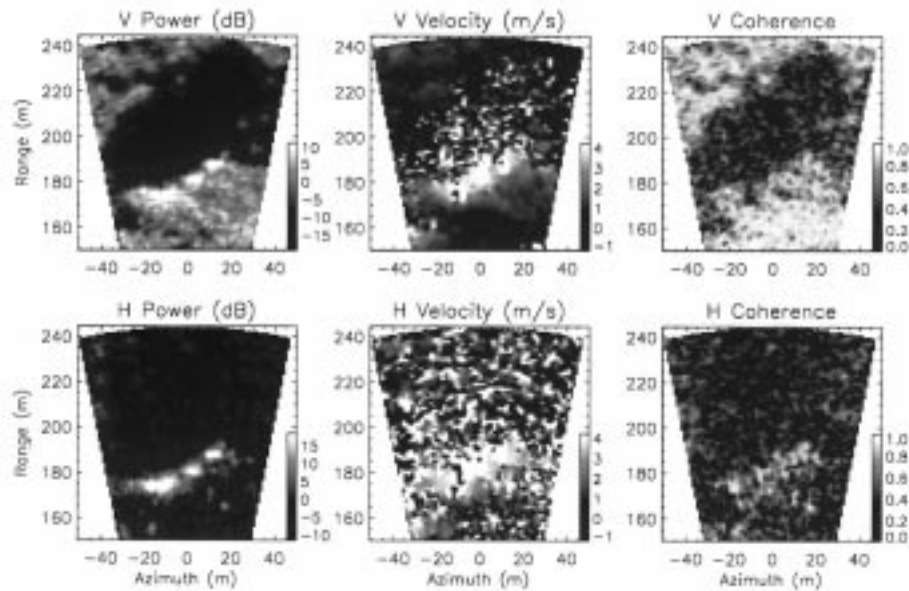
(a)
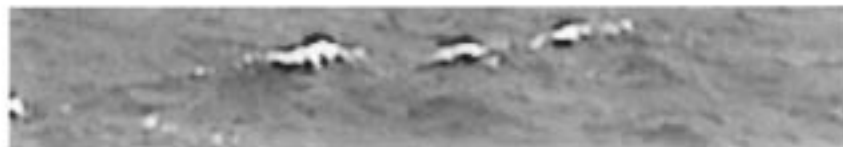
(b)

(c)

Fig. 5. Radar and video images for an upwind, developed sea (Case C). (a) Radar images. (b) Stretched video images. (c) Color-composite of radar images in video coordinates.

somewhat weaker, but more symmetric H distribution. The asymmetry of the V distributions can be attributed to two primary factors: 1) modulation transfer function [23] and shadowing effects and 2) contributions due to non-Bragg scatterers that appear preferentially near wave crests. In the absence of any amplitude modulation or shadowing effects, the velocity distribution observed would simply represent the distribution of wave orbital velocities projected in the radar line-of-sight, which would be reasonably symmetric for the long waves. The geometrical component of the MTF predicts and field measurements support backscatter favoring the portions of waves oriented toward the radar that yield smaller local incidence angles [24], [25].

V peaks are displaced from zero Doppler by about 0.5 ms^{-1} consistent with contributions due to the phase velocities of Bragg-resonant capillary waves (0.24 ms^{-1}) and the effects of wind-induced surface current, typically about 3% of the wind speed [26]. Though the locations of the V peaks remain fairly constant, the width varies with the sea state. The young seas

has a narrower distribution than the developed sea consistent with the observation that shorter waves characteristic of young seas have smaller orbital velocities than do the larger waves of developed seas. Horizontal lines in the plots indicate expected standard deviations of orbital velocities due to the long waves as estimated from the rms wave height and dominant wave frequencies of Table I. These estimates assume a Gaussian distribution of velocities and show good agreement with the widths of the distributions with the exception of Case A. This may be an effect of residual swell and differences in record lengths used between radar and wave-wire measurements. For the decaying sea, the intensity of the backscatter is much weaker than the other two cases due to the reduced energy in the capillary waves as winds diminish.
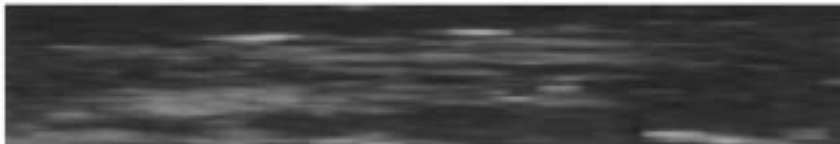
The location of the H-distribution peaks are of consistently higher velocity than the corresponding V peaks. For the young sea, the distribution is generally confined to a range of velocities around 1.8 ms^{-1}. For the developed sea the distribution is centered at a higher velocity 2.4 ms^{-1}, but is also much
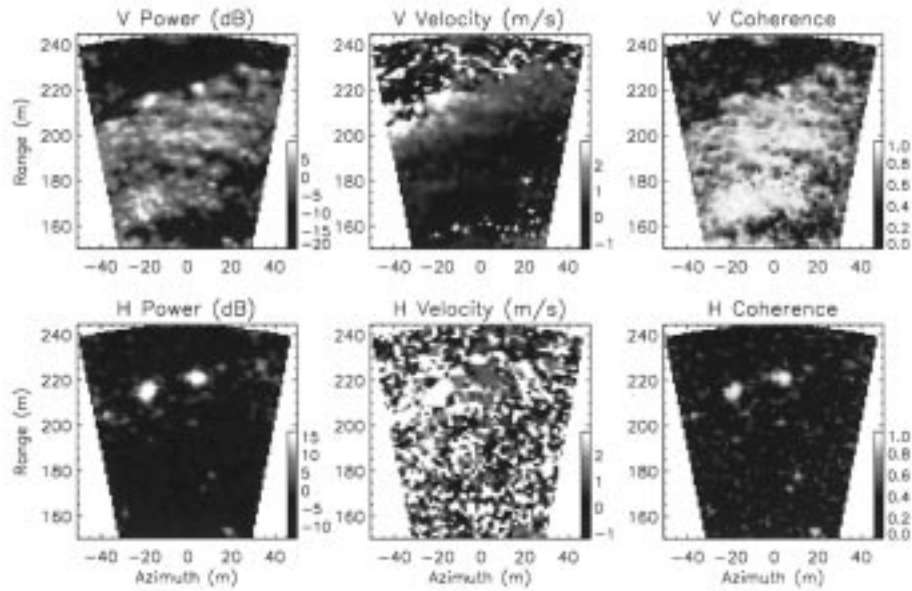
(a)

(b)

(c)

Fig. 6.   Same as Fig. 5 for an upwind decaying sea (Case D).

broader, encompassing a wider range of velocities. In Case C, significant Doppler foldover is evident. The total backscattered power for young and developed seas are comparable and are greater than that for the decaying sea.

C. Doppler Properties of Sea Spikes

Visual inspection of the H and V radar images of Figs. 3–7 show that the discrete scatterers observed in H images often appear in the V images as well. These events in the V imagery show impulsive characteristics with large Doppler shifts indicating a non-Bragg component to the V polarized backscatter. However, because the Bragg component of backscatter for V is generally much stronger than that for H, these events do not stand out as much in V radar images or in Doppler distributions.

In the remainder of this paper, we focus on the nature of these sea-spike events in radar imagery. To this end, we begin by conditionally sampling imagery based on the presence of a detectable signal in the H channel. To discriminate between signal-dominated and noise-dominated pixels in H-backscatter images, both a power threshold and a coherence criterion are used. The power threshold accepts all pixels whose power is at least 10 dB above the mean noise level, while the coherence is used to discriminate signal-dominated pixels at lower SNR's. Fig. 9 shows a histogram of observed H coherencies for Case B (solid line). Superimposed is a power-weighted version of the same histogram (dashed line) or the distribution of power as a function of coherence. Taken together, these curves indicate two populations of pixels with a dividing line occurring roughly near $\rho = 0.8$. The larger population of lower coherence pixels is generally noise-dominated, so we also choose to accept all pixels whose coherence exceeds 0.8. A cumulative histogram of filtered H-polarized backscatter is shown in Fig. 9 plotted on Rayleigh probability axes [27]. H-polarized LGA backscatter is often described in terms of the Weibull distribution, whose cumulative distribution function (CDF) is given by $F(x) = 1 - \exp(x^B/A)$. Plotting $10 \log_{10}\{-\log[1 - F(x)]\}$ versus power in dB allows one
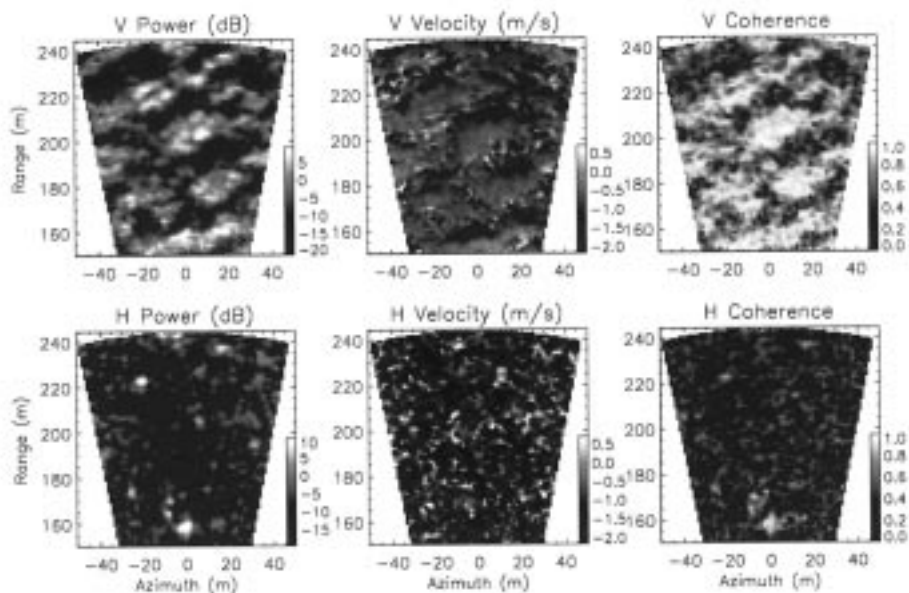
(a)

(b)

(c)

Fig. 7. Same as Fig. 5 for a downwind orientation (Case A).

to estimate the shape parameter, B through the slope of the resulting curve. The tail of this particular distribution is given by $B = 0.67$.

Fig. 10 shows Doppler distributions consisting only of pixels identified as signal dominated. While the conditional sampling has not changed, the H distribution's shape much from that of the original, much of the energy has been removed from the V distribution, which now appear more similar to the H. The mean velocities of the V distributions are still systematically lower than the H, likely indicating significant contributions of Bragg scattering within the resolution cells containing non-Bragg scatterers. In such a case, the mean velocity reported represents a power-weighted average due to the competing scattering mechanisms within the pixel. When considering polarization ratios with respect to non-Bragg scattering models, it is important to minimize the influence of residual Bragg scattering contributions to the V polarized return. The relative impact of such Bragg scattering would be greatest in the smaller amplitude sea spikes. If we consider only the upper half of available H pixels (those H pixels with power exceeding the median power), then the corresponding V Doppler-distribution approach the H distribution more closely as indicated in Fig. 10 where most of the energy discarded is from the lower velocities. Scatter diagrams of V velocities versus H velocities for these pixels indicate that although some velocity bias is still present, the correlation of V velocities with H velocities is reasonably high. We note here that although only half of the data points have been retained at this point, these represent about 90% of the detected H-polarized signal power.

Fig. 11 shows histograms of the polarization ratio H/V evaluated on a pixel-by-pixel basis. We find the most probable polarization ratio to be in the neighborhood of 5 dB for the young and developed seas, a few decibels higher for decaying seas, and a few decibels lower for the downwind look. Thus, for the sea spikes observed, polarization ratios exceed unity most of the time. Because of residual influences of V-polarized Bragg backscatter within the resolution cells, polarization
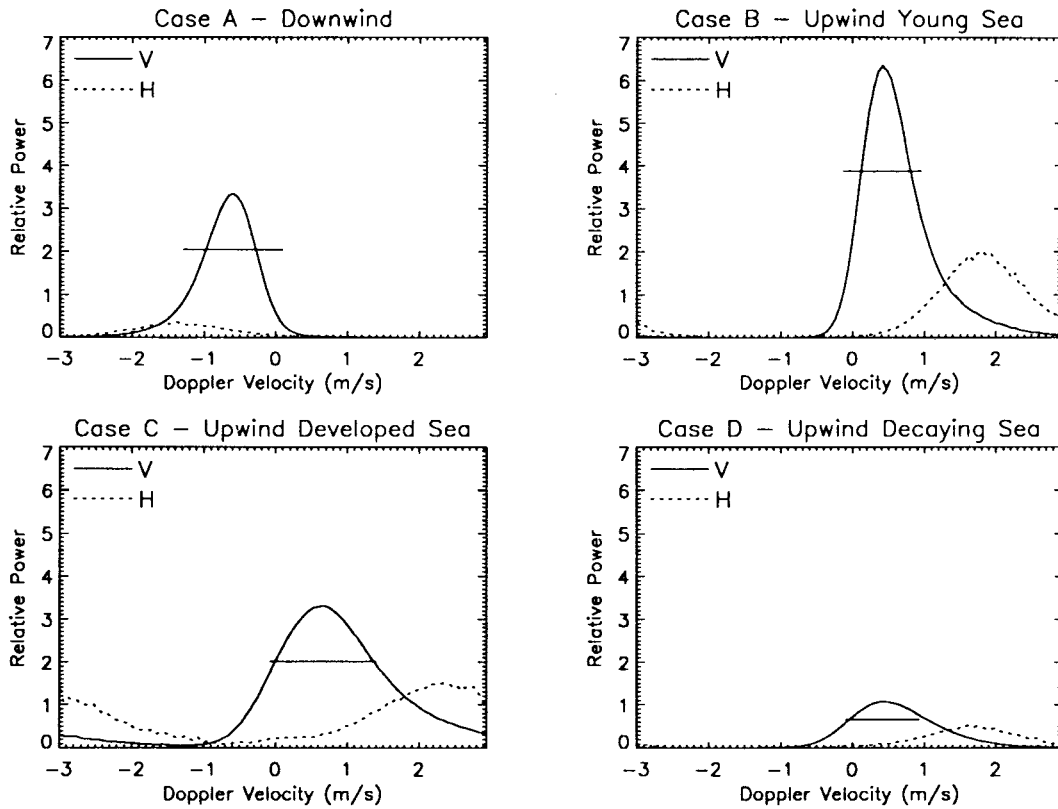
Fig. 8. Weighted Doppler distributions of V backscatter (solid lines) and H backscatter (dashed lines) for the four cases studied. Horizontal lines mark the standard deviations of orbital velocities as estimated from sea-truth data.

ratios reported here likely underestimate the "true" polarization ratio of the non-Bragg component of scattering alone. This might partially explain the noticeably higher polarization ratios observed for the decaying sea (Case D) where winds are low and Bragg backscatter levels are reduced.

IV. COMPARISON WITH VIDEO

To determine any relation of scattering signatures to surface geometries, we attempt to correlate sea spikes in the radar images with surface features evident in video recordings of the surface. The primary intent of this analysis is twofold: first, to determine if visually different surface features show measurably distinct Doppler or polarization ratio properties, and second, to determine to what extent the radar signature is a metric of visual whitecapping. During the experiment, both video recordings and radar data were synchronized using an IRIG-B time code generator that stamped both the video and radar images with the current time. Following the experiment, a representative sampling of 100 video images spanning the duration of each radar record was extracted using a frame grabber. Using the time stamps on each video image, we retrieved the corresponding radar images for comparison.

Radar sea-spike images were compared with video images and scattering events were divided into four classes: I) white-capping exclusively present; II) "steep" wave feature present, but no whitecap; III) both a combination of whitecapping and steep waves; and IV) no feature visibly evident. Classes I) and II) are unambiguous, while Class III) was included to account for spatially large sea-spike events corresponding to long-

crested partially breaking waves. The intent is to discriminate unambiguously between strictly whitecapping and steep waves with the expectation that properties of Class III) will fall somewhere in between. Once categorized, radar image pixels comprising these event types are selectively examined to infer mean Doppler and polarization ratio properties.

Given the $32° \times 24°$ field-of-view of the video camera and the 640×480 pixel resolution of the frame grabber, the angular sampling resolution of the video image is approximately $0.05°$. With this information, as well as the nominal height of the array above the mean water level and the horizon as a reference, the radar's range versus azimuth image is mapped into the video's elevation versus azimuth image. The radar's azimuthal resolution is $0.05°$, a factor of ten lower than the video sampling resolution. In elevation, however, the video angular resolution maps to range resolutions of 1.6 to 4 m at ranges of 150 and 246 m, respectively. These are comparable to or slightly lower than that of the radar.

A limitations inherent to this kind of comparison needs to be mentioned. At near-grazing incidence, pixel-by-pixel classification is *extremely* difficult due to inevitable misregistration between radar and video images due to the undulating sea surface (the assumption of a flat sea surface must be made in order to transform between radar and video coordinates). This demanded that classification be performed manually on an "event-by-event" basis where an event is defined as a group of contiguous sea-spike image pixels. To make manual classification of the pixels reasonable, it was necessary to place a modest requirement on the spatial extent of events. Thus, beginning
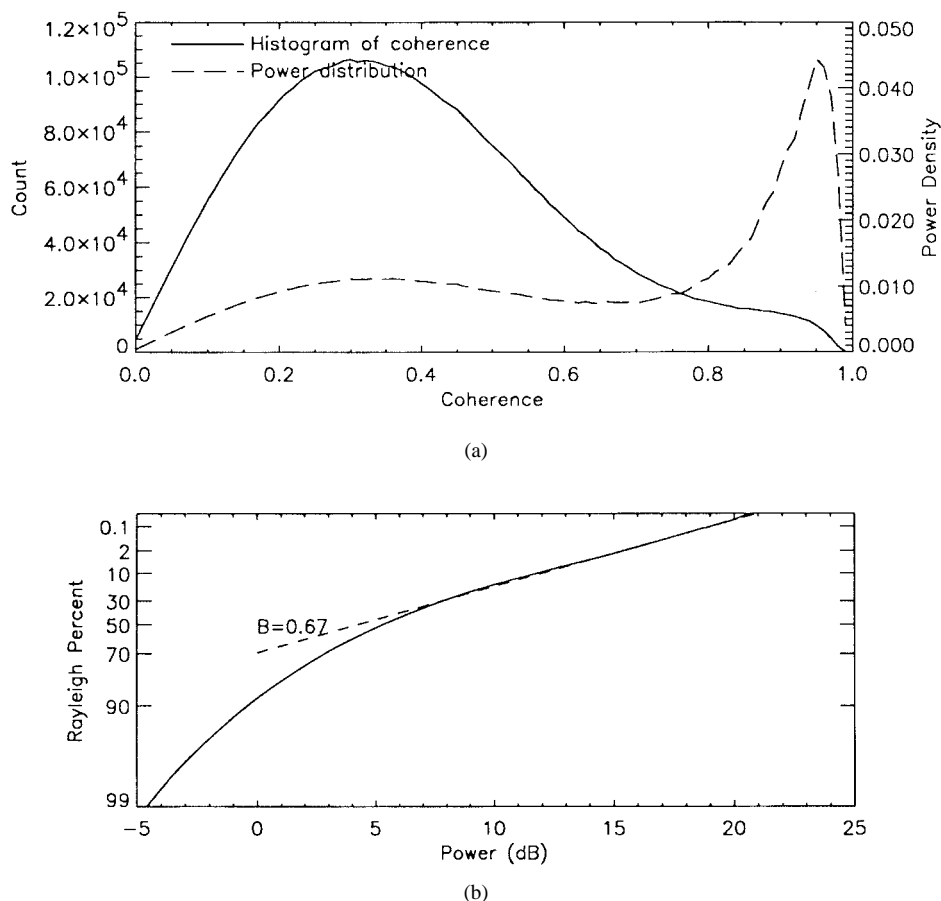
Fig. 9. (a) Histogram of coherence and the distribution of power with coherence indicate two populations of image pixels (signal and noise). (b) Cumulative histogram of H-polarized backscatter on Rayleigh axes. A fit to the tail of the distribution indicates a Weibull distribution with a shape parameter of 0.67. The power scale is normalized to the mean V-pol Bragg backscatter level.
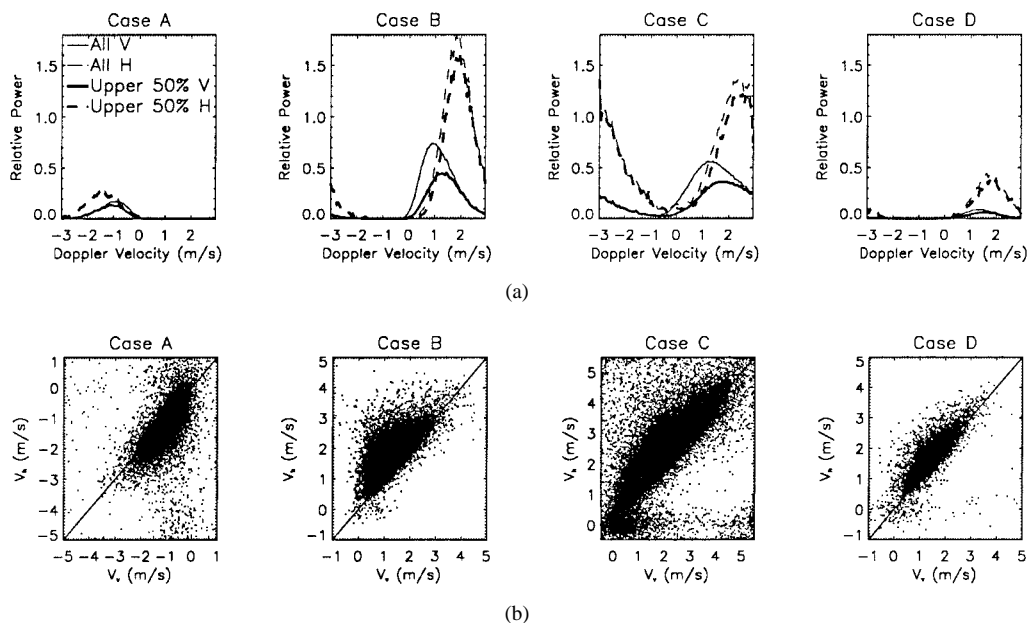
Fig. 10. (a) Doppler distributions for sea-spike pixels. The solid lines are V pol, dashed lines are H pol. Thin lines are the distributions for all sea-spike pixels and thick lines are the distributions for pixels whose H backscatter exceeds the median (upper 50%). (b) Scatter plots of V-pol versus H-pol Doppler velocity for upper 50% of pixels.

with the upper half of H-pixels, only those events whose spatial extent exceeded two contiguous pixels were considered.

Though these conditions may seem somewhat arbitrary, they discard only the events for which visual comparison is not
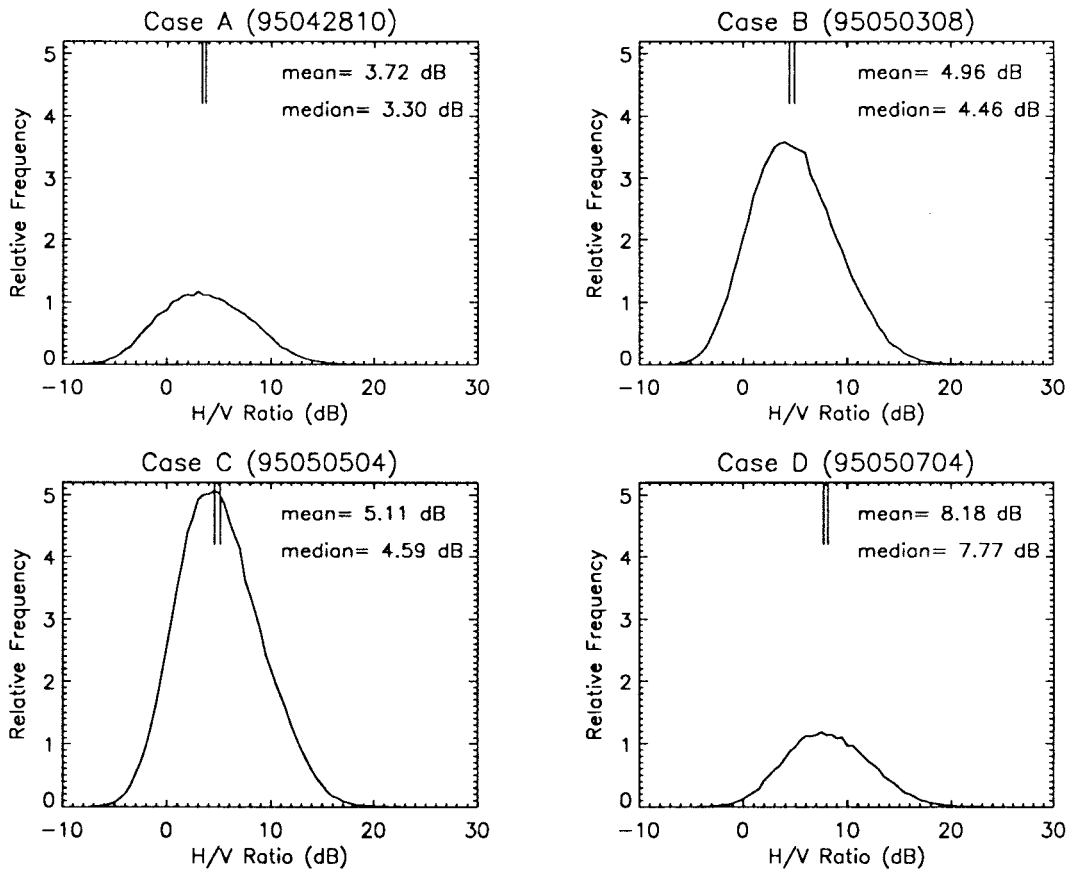
Fig. 11.   Polarization ratio histograms for upper 50% of sea-spike pixels indicate polarization ratios generally greater than unity. Noticeably higher polarization ratios for Case D may be due to the reduced influence of Bragg scattering for V polarization under the low wind conditions.

straightforward while retaining most of the total H-polarized signal power (85–90%). We believe this to be as inclusive a criterion as is tractable.

Results of the classification are shown in Fig. 12 and Table II. Stacked bar charts in the figure show the fractional contributions of each class. The table lists the number of events classified for each case and the mean power, Doppler velocity, and polarization ratio statistics. For the young and the developed sea (Cases B and C), video and radar comparison show that Classes I) and III), corresponding to total or partial whitecapping, together account for about 30% of the observed sea-spike events while steep wave features account for approximately 60%. For the decaying sea (Case D) there were virtually no whitecaps despite the presence of large waves. In this case, total or partial whitecapping accounted for about 3% of observed spikes while steep features accounted for 92%. For the downwind look (Case A), a somewhat larger percentage of the sea-spike events (about 40%) can be associated with actively breaking waves. Though both the number of spikes and their intensity are significantly lower than for upwind looks, this viewing geometry appears to suppress the influence of steep features.

These percentages are based solely on event counts with no regard to their intensity. If events are weighted by their spatial coverage, the percentage attributable to whitecapping increases somewhat. If events are weighted by their corresponding
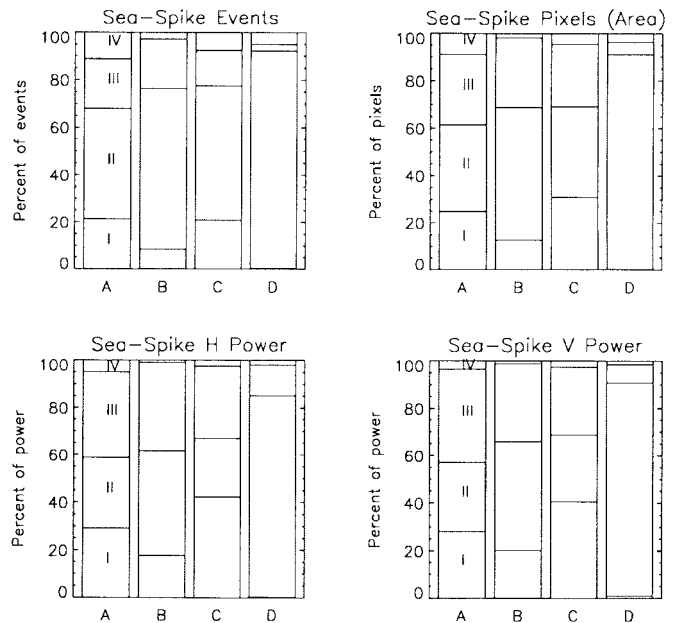

Fig. 12.   Distributions of sea-spike classes for each case. Percentages are shown in terms of number of events, pixels (area), and total V and H power. Class I) whitecaps, Class II) "steep" features, Class III) both whitecaps and steep features, Class IV) no feature evident.

powers, actively breaking waves (categories I and III) can be associated with a modest majority of power in Cases A,

TABLE II
RESULTS OF SEA-SPIKE CLASSIFICATION P_V AND P_H ARE BACKSCATTERED POWERS FOR V AND H SEA SPIKES
(NORMALIZED TO THE MEAN V-BRAGG BACKSCATTER LEVEL), V_V AND V_H ARE DOPPLER DISTRIBUTION CENTROIDS,
H/V IS THE MEDIAN POLARIZATION RATIO, Λ_{Vh} IS THE OCEAN WAVE LENGTH WITH A PHASE SPEED EQUAL TO V_H

Case	Class	# events	P_v (dB)	P_h (dB)	V_v (ms^{-1})	V_h (ms^{-1})	H/V (dB)	Λ_{Vh} (m)
A	I	51	9.08	12.92	-1.44	-1.67	3.28	1.8
	II	112	6.72	10.58	-1.27	-1.52	3.47	1.5
	III	50	8.71	11.95	-1.45	-1.76	2.67	
	IV	27	4.63	10.41	-1.10	-1.13	5.78	
B	I	72	8.44	13.77	2.18	2.50	4.66	4.0
	II	585	6.05	11.58	1.19	1.66	4.67	1.8
	III	181	7.31	13.44	1.69	2.19	5.11	
	IV	24	5.86	12.19	1.25	1.58	6.04	
C	I	173	7.96	13.32	2.85	3.29	4.69	6.9
	II	470	5.30	10.28	1.49	1.95	4.36	2.4
	III	124	6.62	12.29	2.27	2.73	4.53	
	IV	63	4.70	10.36	1.52	2.14	5.07	
D	I	1	12.66	16.18	3.18	3.72	3.00	8.9
	II	257	7.71	15.99	1.51	1.72	8.10	1.5
	III	8	9.29	18.18	1.85	2.30	7.60	
	IV	14	4.71	14.20	0.71	0.77	9.83	

B, and C even though they account for a minority of events. In decaying seas, steep features still dominate the sea-spike signature.

Doppler properties of classified sea-spike events are summarized in Fig. 13. Here, Doppler distributions and polarization ratio histograms are computed individually for each class. Examining the Doppler signatures it is possible to discriminate between the velocity distributions of categories I and II. Mean Doppler shifts for whitecapping events are generally higher than for steep wave features, although there is significant overlap of the two distributions. Also, the Doppler distributions for category III fall between I and II as expected. This is true for both V and H polarizations.

It was our expectation that actively breaking waves and steep features as observed on the open ocean might show noticeably different polarization ratios. Comparing the polarization ratios for scatterers in Classes I) and II), however, we do not observe a significant difference in the mean-polarization ratios (see Table I). The distributions for both classes are again highly overlapped as was the case for the Doppler signatures. Based upon these observations, it appears that polarization ratio is less sensitive to the class of scatterer than is Doppler velocity, at least on the open ocean. Differences are evident in the mean power of events of Classes I) and II) for both vertical and horizontal polarizations. Table II shows mean differences on the order of 2 dB. Again, however, distributions for both (not shown) are highly overlapped.

V. DISCUSSION

Though virtually every investigation of high-resolution ocean surface backscatter has noted the importance of breaking waves in the horizontally polarized signature, few have deliberately attempted to correlate microwave echoes with whitecap events using video imaging in the field. Lewis and Olin [8] used combined radar and video in their investigation of breaking waves in the near-shore zone. They noted an obvious correspondence between the largest events and breaking, but also noted a large number of events not associated with visual breaking. Wave breaking in shallow water characterized by large "plunging" breakers is quite different than breaking in deep water characterized more by "spilling" breakers.

Jessup *et al.* [20] used combined scatterometer and video measurements from a tower to determine whitecap detection estimates. At the moderate incidence angle they employed, the "sea spikes" they detected were dominated more by specular events where H/V $\approx$ 1. Using a combination of power and Doppler criteria to identify sea spikes associated with whitecaps and, with a space-time window included in their comparison, they found they could detect 60–70% of sea spikes produced by waves which eventually broke within a limited distance downwave of their illuminated area. If they limited attention to coincident sea-spike and whitecap events, detection probabilities were substantially lower.

We found (for the admittedly limited number of cases studied) that the majority of observed large sea spikes are not associated with visible whitecaps, though whitecaps appear responsible for a modest majority of the total sea-spike power. Since the radar images an extended area over time, it would be inappropriate to include a similar space-time window about our radar measurements to improve detection statistics. That is, at any given time the radar image consists of echoes due both to actively breaking waves and to steep waves, which may or may not evolve to breaking themselves. On average, however, the actively breaking waves and the portion of steep waves that do eventually break should exist in proportion to their relative lifetimes. From wavetank measurements, it is generally believed that the most intense part of the sea-spike signature is associated with the unstable steep-crested phase of breaking just prior to the whitecapping event itself [10], [16], [28]. Sea-spike decorrelation times of the order of 500 ms (reported in [11]) suggest the approximate duration of the relevant phases of breaking for sea spikes. Thus, one might expect that the average number of steep waves, observed at a given instant, that evolve to breaking is somewhat smaller than the average number of visible whitecap events. The large proportion of sea spikes due to steep features we observe supports the notion of a large population of steep, but non-visibly breaking waves contributing to the overall H polarized
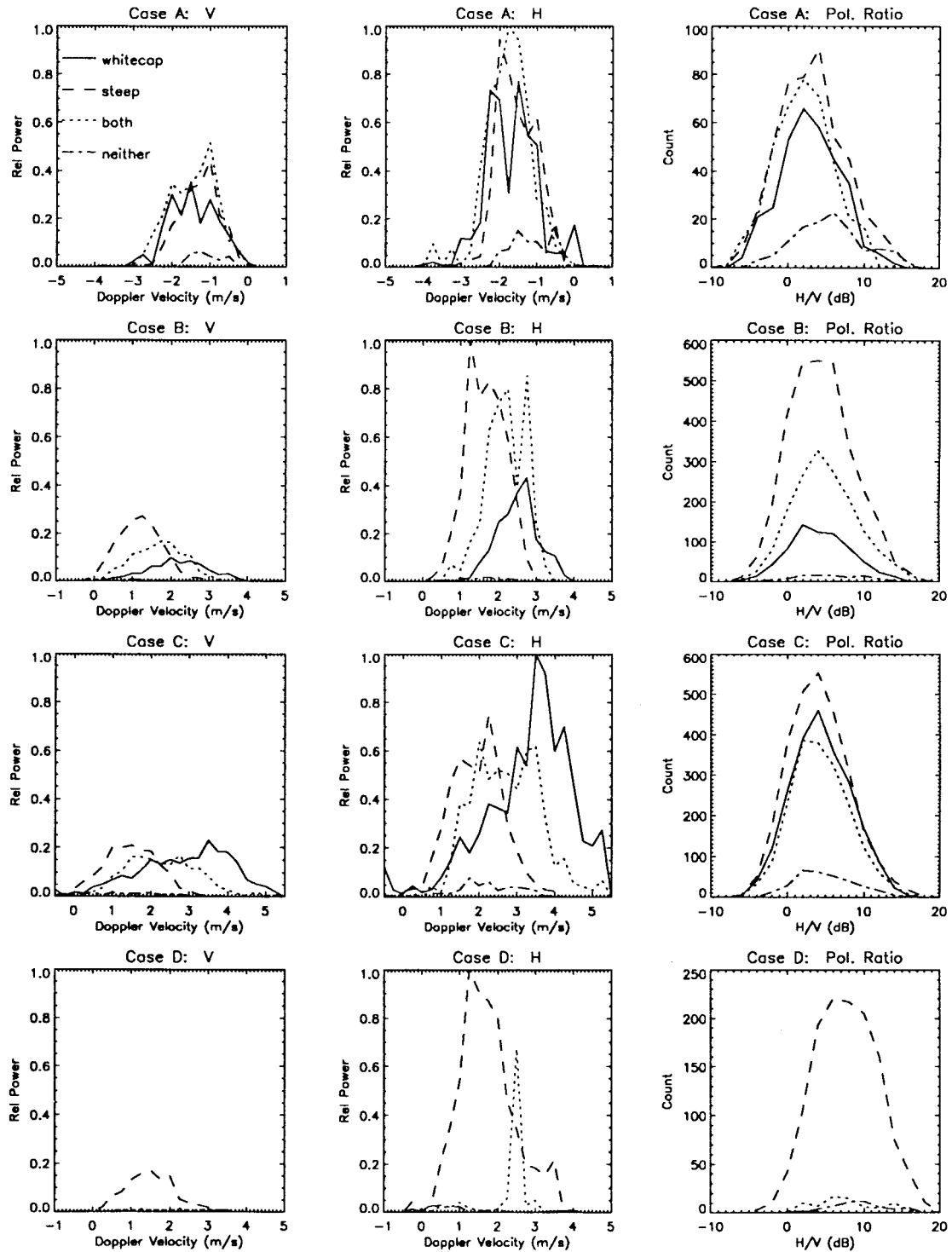
Fig. 13. Doppler and polarization ratio properties of individual classes for each case (top to bottom). Shown are Doppler distributions for V-polarized (left) and H-polarized (middle) backscatter and polarization ratio histograms (right).

return. A significant fraction of these are likely the "microscale breakers" described by Banner and Peregrine [31]—small wave crests less than about 4 cm high in which surface tension is sufficiently strong to prevent air entrainment and, hence, visible whitecapping. Since this scale is comparable to the X-band radar's electromagnetic wavelength (3 cm), features on this scale could be rather efficient scatterers. The spatial

resolution of our radar and video measurements does not permit an assessment of the relative impact of these events.

Given the comparable contributions of scattering power from steep waves and whitecaps in Cases A, B, and C, it is also apparent that the mean velocity of visual breaking is likely underestimated by the centroid of the H Doppler spectrum. Lee *et al.* [7] described their LGA scattering measurements

in terms of "slow" and "fast" scatterers as discerned from Doppler spectra. The fast scatterers they associated with non-Bragg scattering from gravity waves. Assuming the mean velocity of the fast scatterers was associated with the phase speed of breaking waves, they inferred their wavelength and found them to be short gravity waves well beyond the spectral peak. Similar observations were made by Smith *et al.* [29] and Frasier and McIntosh [30] who estimated breaking wavelength from the apparent group velocity of radar modulations associated with non-Bragg scatterers that were evident in dispersion $(\omega - k)$ diagrams. Our results indicate that the H Doppler spectrum includes roughly equal contributions from actively breaking waves and from steep features. Because the observed "steep wave" spikes tend toward lower average Doppler velocities, their influence on the Doppler spectrum may bias any estimates of the wavelength of (large-scale) breaking toward shorter waves. The last column of Table II lists the wavelength of ocean waves whose phase velocity is equal to the mean H-Doppler velocities of Classes I) and II). These should be compared with the dominant wavelengths of Table I.

Though we have restricted our attention to the larger events in the radar/video comparison, the substantial overlap in both the power distributions and the Doppler velocity distributions for steep wave spikes and for whitecaps indicate that attempting to discriminate between the two is not straightforward. One cannot detect a reasonable range of breaking scales without also detecting steep wave features, at least using the parameters of power, polarization ratio, and Doppler velocity. It is perhaps more realistic to consider a simple parameter like sea-spike coverage based solely on a power threshold. Though it may be consistently higher than separate estimates of whitecap coverage, it might scale with wind speed or wind stress in the same way. Phillips [32] argued as much on dimensional grounds, predicting a cubic dependence on the number of sea spikes with wind stress. Such a dependence was also observed by Jessup *et al.* in their moderate incidence angle tower-based measurements [21]. Investigating these relationships for our measurements is an area of future efforts.

ACKNOWLEDGMENT

REFERENCES

[1] J. W. Wright, "A new model for sea clutter," *IEEE Trans. Antennas Propagat.,* vol. AP-16, pp. 217–223, Mar. 1968.

[2] W. J. Plant, "Bragg scattering of electromagnetic waves from air/sea interface," in *Surface Waves and Fluxes,* G. L. Geernaert and W. J. Plant, Eds. Norwell, MA: Kluwer, 1990, vol. II.

[3] V. W. Pidgeon, "Doppler dependence of radar sea return," *J. Geophys. Res.,* vol. 73, pp. 1333–1341, 1968.

[4] N. W. Guinard, J. T. Ransone, Jr., and J. C. Daley, "Variation of the NRCS of the sea with increasing roughness," *J. Geophys. Res.,* vol. 76, pp. 1525–1538, 1971.

[5] A. I. Kalmykov and V. V. Pustovoytenko, "On polarization features of radio signals scattered from the sea surface at small grazing angles," *J. Geophys. Res.,* vol. 81, pp. 1960–1964, 1976.

[6] D. B. Trizna, "A model for Doppler peak spectral shift for low grazing angle sea scatter," *IEEE J. Oceanic Eng.,* vol. OE-10, pp. 368–375, Oct. 1985.

[7] P. H. Y. Lee, J. D. Barter, K. L. Beach, C. L. Hindman, B. M. Lake, H. Rungaldier, J. C. Shelton, A. B. Williams, R. Yee, and H. C. Yuen, "X band microwave backscattering from ocean waves," *J. Geophys. Res.,* vol. 100, pp. 2591–2611, 1995.

[8] B. L. Lewis and I. D. Olin, "Experimental study and theoretical model of high-resolution radar backscatter from the sea," *Radio Sci.,* vol. 15, pp. 815–828, 1980.

[9] A. T. Jessup, W. C. Keller, and W. K. Melville, "Measurements of sea spikes in microwave backscatter at moderate incidence," *J. Geophys. Res.,* vol. 95, pp. 9679–9688, 1990.

[10] D. S. W. Kwoh and B. M. Lake, "A deterministic, coherent, and dual-polarized laboratory study of microwave backscattering from water waves—Part I: Short gravity waves without wind," *IEEE J. Oceanic Eng.,* vol. OE-9, pp. 291–308, Dec. 1984.

[11] D. B. Trizna, J. P. Hansen, P. Hwang, and J. Wu, "Laboratory studies of radar sea spikes at low grazing angles," *J. Geophys. Res.,* vol. 96, pp. 12529–12537, 1991.

[12] J. D. Barter and P. H. Y. Lee, "Polarimetric optical imaging of scattering surfaces," *Appl. Opt.,* vol. 35, pp. 6015–6027, 1996.

[13] D. R. Lyzenga, A. L. Maffett, and R. A. Schuchman, "The contribution of wedge scattering to the radar cross section of the ocean surface," *IEEE Trans. Geosci. Remote Sensing,* vol. GRS-21, pp. 502–505, Oct. 1983.

[14] L. B. Wetzel, "On microwave scattering by breaking waves," in *Wave Dynamics and Radio Probing of the Ocean Surface,* O. M. Phillips and K. Hasselmann, Eds. Norwell, MA: Kluwer, 1986.

[15] A. D. Rozenberg and W. K. Melville, "Laboratory study of the fine structure of breaking waves for scatterometry applications," in *Proc. Int. Geosci. Remote Sensing Symp.,* Lincoln, NE, May 1996, pp. 2204–2206.

[16] M. A. Sletten, D. B. Trizna, and J. P. Hansen, "Ultrawide-band radar observations of multipath propagation over the sea surface," *IEEE Trans. Antennas Propagat.,* vol. 44, pp. 646–651, May 1996.

[17] R. E. McIntosh, S. J. Frasier, and J. B. Mead, "FOPAIR: A focused array imaging radar for ocean remote sensing," *IEEE Trans. Geosci. Remote Sensing,* vol. 33, pp. 115–124, Jan. 1995.

[18] K. S. Miller and M. M. Rochwarger, "A covariance approach to spectral moment estimation," *IEEE Trans. Inform. Theory,* vol. IT-18, pp. 588–596, May 1972.

[19] R. J. Doviak and D. S. Zrnić, *Doppler Radar and Weather Observations.* New York: Academic, 1984.

[20] A. T. Jessup, W. K. Melville, and W. C. Keller, "Breaking waves affecting microwave backscatter—1: Detection and verification," *J. Geophys. Res.,* vol. 96, pp. 20 547–20 559, 1991.

[21] ———, "Breaking waves affecting microwave backscatter—2: Dependence on wind and wave conditions," *J. Geophys. Res.,* vol. 96, pp. 20 561–20 569, 1991.

[22] N. M. Blachman and G. A. McAlpine, "The spectrum of a high-index waveform: Woodward's theorem revisited," *IEEE Trans. Commun. Technol.,* vol. CT-17, pp. 201–208, Apr. 1969.

[23] W. J. Plant, "The modulation transfer function: Concept and applications," *Radar Scattering From Modulated Wind Waves,* G. J. Komen and W. A. Oost, Eds. Norwell, MA: Kluwer, 1989.

[24] W. C. Keller, W. J. Plant, R. A. Petitt, Jr., and E. A. Terray, "Microwave backscatter from the sea: Modulation of received power and Doppler bandwidth by long waves," *J. Geophys. Res.,* vol. 99, pp. 9751–9766, 1994.

[25] E. M. Poulter, M. J. Smith, and J. A. McGregor, "Microwave backscatter from the sea surface: Bragg scattering by short gravity waves," *J. Geophys. Res.,* vol. 99, pp. 7929–7943, 1994.

[26] J. Wu, "Wind induced drift currents," *J. Fluid Mech.,* vol. 68, pp. 49–70, 1975.

[27] D. B. Trizna, "Statistics of low grazing angle radar sea scatter for moderate and fully developed ocean waves," *IEEE Trans. Antennas Propagat.,* vol. 39, pp. 1681–1690, Dec. 1991.

[28] M. R. Loewen and W. K. Melville, "Microwave backscatter and acoustic radiation from breaking waves," *J. Fluid Mech.,* vol. 224, pp. 601–623, 1991.

[29] M. J. Smith, E. M. Poulter, and J. A. McGregor, "Doppler radar measurements of wave groups and breaking waves," *J. Geophys. Res.,* vol. 101, pp. 14269–14282, 1996.

[30] S. J. Frasier and R. E. McIntosh, "Observed wavenumber-frequency properties of microwave backscatter from the ocean surface at near-grazing angles," *J. Geophys. Res.,* vol. 101, pp. 18 391–18 407, 1996.

[31] M. L. Banner and D. H. Peregrine, "Wave breaking in deep water," *Annu. Rev. Fluid Mech.,* vol. 25, pp. 373–398, 1993.

[32] O. M. Phillips, "Radar returns from the sea surface—Bragg scattering and breaking waves," *J. Phys. Oceanography,* vol. 18, pp. 1065–1074, 1988.

Yong Liu (S'93–M'98) received the B.S. degree from the Massachusetts Institute of Technology, Cambridge, in 1992, and the Ph.D. degree from the University of Massachusetts, Amherst, in 1997, both in electrical engineering.

From 1992 to 1997, he was a Research Assistant at the Microwave Remote Sensing Laboratory at the University of Massachusetts, involved in the development of the focused phased-array imaging radar and the analysis of ocean remote sensing data. He is currently a member of Technical Staff in the Radar Science and Engineering Section at the Jet Propulsion Laboratory, Pasadena, CA, working on the sea-winds scatterometer and related project.

Stephen J. Frasier (S'94–M'95) received the B.E.E. degree from the University of Delaware, Newark, in 1987, and the Ph.D. degree from the University of Massachusetts, Amherst, in 1994.

From 1987 to 1990, he worked for SciTec, Inc. (a subsidiary of TRW), Princeton, NJ, on various signal processing applications for missile and laser detection. From 1990 to 1994 he was a Research Assistant in the Microwave Remote Sensing Laboratory, University of Massachusetts, Amherst, where he developed the FOPAIR imaging radar and performed initial measurements of ocean surface waves. From 1994 to 1997 he continued his work as a Research Engineer and Senior Research Fellow and since 1997 he has worked as an Assistant Professor in the Department of Electrical and Computer Engineering at the same university. His research interests include microwave and millimeter-wave imaging and interferometry, radar and radiometer systems, radio oceanography, and radar meteorology. He currently directs research projects in microwave imaging of the ocean surface, airborne measurement of ocean surface current, and imaging of atmospheric boundary-layer turbulence at UHF.

Dr. Frasier is a member of the American Meteorological Society, URSI Commission F, Tau Beta Pi, and Eta Kappa Nu.

Robert E. McIntosh (S'66–M'67–SM'72–F'85) received the B.S. degree (electrical engineering) from the Worcester Polytechnic Institute, Worcester, MA, in 1962, the M.S. degree from Harvard University, Cambridge, MA, in 1964, and the Ph.D. degree from the University of Iowa, Iowa City, in 1967.

He was a member of the technical staff of Bell Telephone Laboratories Inc., N. Andover, MA, from 1962 to 1965. In 1967 he joined the Department of Electrical and Computer Engineering at the University of Massachusetts, Amherst, where he is now a Distinguished University Professor. He served as Coordinator of the Microwave Electronics Group at the University of Massachusetts from 1981 to 1987 and now codirects the Microwave Remote Sensing Laboratory there. He founded Quadrant Engineering, Inc., Amherst, MA, in 1982 (with C. T. Swift). His teaching and research interests are in electromagnetic field theory, microwave engineering, wave propagation, and remote sensing.

Dr. McIntosh is a recipient of the IEEE Centennial Medal. He was elected to the National Academy of Engineering in 1997. He received the Senior Faculty Scholarship Award from the College of Engineering Alumni (1984), the General Electric Teaching Award (1988), and various ECE department teaching awards. He was selected as a speaker for the University's Distinguished Faculty Lecture Series in 1992 and was awarded a University Research Fellowship in 1995. He also received the Hobart Newell Award from Worcester Polytechnic Institute. He is a past president of the IEEE Geoscience and Remote Sensing Society (1984) and the Antennas and Propagation Society (1985). He received the Distinguished Service Award in 1985 and the Distinguished Achievement Award in 1997 from the Geosciences and Remote Sensing Society. He was also a member of the United States National Committee of URSI from 1984 to 1992. He has served as editor-in-chief of the IEEE TRANSACTIONS ON ANTENNAS AND PROPAGATION and as a guest editor for special issues of the IEEE TRANSACTIONS ON GEOSCIENCE AND REMOTE SENSING, IEEE TRANSACTIONS ON EDUCATION, and IEEE PROCEEDINGS.

射 频 和 天 线 设 计 培 训 课 程 推 荐

易迪拓培训(www.edatop.com)由数名来自于研发第一线的资深工程师发起成立，致力并专注于微波、射频、天线设计研发人才的培养；我们于 2006 年整合合并微波 EDA 网(www.mweda.com)，现已发展成为国内最大的微波射频和天线设计人才培养基地，成功推出多套微波射频以及天线设计经典培训课程和 ADS、HFSS 等专业软件使用培训课程，广受客户好评；并先后与人民邮电出版社、电子工业出版社合作出版了多本专业图书，帮助数万名工程师提升了专业技术能力。客户遍布中兴通讯、研通高频、埃威航电、国人通信等多家国内知名公司，以及台湾工业技术研究院、永业科技、全一电子等多家台湾地区企业。

易迪拓培训课程列表：http://www.edatop.com/peixun/rfe/129.html

射频工程师养成培训课程套装

该套装精选了射频专业基础培训课程、射频仿真设计培训课程和射频电路测量培训课程三个类别共 30 门视频培训课程和 3 本图书教材；旨在引领学员全面学习一个射频工程师需要熟悉、理解和掌握的专业知识和研发设计能力。通过套装的学习，能够让学员完全达到和胜任一个合格的射频工程师的要求…

课程网址：http://www.edatop.com/peixun/rfe/110.html

ADS 学习培训课程套装

该套装是迄今国内最全面、最权威的 ADS 培训教程，共包含 10 门 ADS 学习培训课程。课程是由具有多年 ADS 使用经验的微波射频与通信系统设计领域资深专家讲解，并多结合设计实例，由浅入深、详细而又全面地讲解了 ADS 在微波射频电路设计、通信系统设计和电磁仿真设计方面的内容。能让您在最短的时间内学会使用 ADS，迅速提升个人技术能力，把 ADS 真正应用到实际研发工作中去，成为 ADS 设计专家…

课程网址： http://www.edatop.com/peixun/ads/13.html

HFSS 学习培训课程套装

该套课程套装包含了本站全部 HFSS 培训课程，是迄今国内最全面、最专业的 HFSS 培训教程套装，可以帮助您从零开始，全面深入学习 HFSS 的各项功能和在多个方面的工程应用。购买套装，更可超值赠送 3 个月免费学习答疑，随时解答您学习过程中遇到的棘手问题，让您的 HFSS 学习更加轻松顺畅…

课程网址：http://www.edatop.com/peixun/hfss/11.html

CST 学习培训课程套装

该培训套装由易迪拓培训联合微波 EDA 网共同推出，是最全面、系统、专业的 CST 微波工作室培训课程套装，所有课程都由经验丰富的专家授课，视频教学，可以帮助您从零开始，全面系统地学习 CST 微波工作的各项功能及其在微波射频、天线设计等领域的设计应用。且购买该套装，还可超值赠送 3 个月免费学习答疑…

课程网址：http://www.edatop.com/peixun/cst/24.html

HFSS 天线设计培训课程套装

套装包含 6 门视频课程和 1 本图书，课程从基础讲起，内容由浅入深，理论介绍和实际操作讲解相结合，全面系统的讲解了 HFSS 天线设计的全过程。是国内最全面、最专业的 HFSS 天线设计课程，可以帮助您快速学习掌握如何使用 HFSS 设计天线，让天线设计不再难…

课程网址：http://www.edatop.com/peixun/hfss/122.html

13.56MHz NFC/RFID 线圈天线设计培训课程套装

套装包含 4 门视频培训课程，培训将 13.56MHz 线圈天线设计原理和仿真设计实践相结合,全面系统地讲解了 13.56MHz 线圈天线的工作原理、设计方法、设计考量以及使用 HFSS 和 CST 仿真分析线圈天线的具体操作，同时还介绍了 13.56MHz 线圈天线匹配电路的设计和调试。通过该套课程的学习，可以帮助您快速学习掌握 13.56MHz 线圈天线及其匹配电路的原理、设计和调试…

详情浏览：http://www.edatop.com/peixun/antenna/116.html

我们的课程优势：

※ 成立于 2004 年，10 多年丰富的行业经验，

※ 一直致力并专注于微波射频和天线设计工程师的培养，更了解该行业对人才的要求

※ 经验丰富的一线资深工程师讲授，结合实际工程案例，直观、实用、易学

联系我们：

※ 易迪拓培训官网：http://www.edatop.com

※ 微波 EDA 网：http://www.mweda.com

※ 官方淘宝店：http://shop36920890.taobao.com